COMPRESSED SENSING FOR SATELLITE CHARACTERIZATION SHADOWING AS A SENSING MATRIX

D. Kobayashi and C. Frueh

Purdue University, School of Aeronautics and Astronautics, 701 W. Stadium Avenue, West Lafayette, IN 47906, USA, Email: {dkobayas, cfrueh}@purdue.edu

ABSTRACT

Characterization is a method to determine the geometric and kinematic properties of an unknown space object. The most straightforward approach is a direct observation by a ground-based telescope, but its applicability is limited to a relatively large object in low Earth orbit. A more versatile method is a light curve inversion scheme, but the shape inversion is challenging for concave objects. This research discusses a potential application of a compressed sensing technique for a resolved image recovery of an unknown satellite, given its non-resolved light curve. Compressed sensing is a signal compression and recovery method that uses a so-called sensing matrix as an encryption key. In a preliminary study, the measurement noise due to the atmosphere is modeled as the sensing matrix, and a resolved image has been recovered. This research has revisited the model and found some limitations. Therefore, an alternative method has been proposed by considering shadow cast on the satellite as the sensing matrix. Two scenarios are investigated: the first scenario models the shadow as a binary random variable while the second scenario uses ray tracing to compute the shadow. In both cases, a net of an unknown satellite has been recovered from its light curve, assuming the shadowing conditions are known. This result implies a great potential of compressed sensing in characterizing space objects that are so remote that traditional resolved imaging is impossible.

Keywords: Characterization; Light Curve; Compressed Sensing.

1. INTRODUCTION

The near-Earth space environment is occupied by over 100 million debris objects greater than 1 mm in size [13]. Although most of the debris objects are fragments that would not appear to be much of a threat, they pose a risk for damaging assets in orbits because of their high orbit energy. The Space Fence system tracks over 200,000 debris objects greater than 1 cm in low Earth orbit to cope with this issue, but many debris objects are yet to be tracked. In this context, it is necessary to detect, track, and characterize new objects to predict their locations at any given time. As a part of this space situational awareness framework, this research focuses on the characterization of unknown space objects.

Several studies have been carried out to observe a satellite by a ground-based telescope directly. The most outstanding example is the FGAN Tracking and Imaging Radar (TIRA), [24] equipped with a high-resolution Ku-band imaging radar. This radar successfully diagnosed the malfunction of the Advanced Earth Observing Satellite (ADEOS) in 1997. Such a direct observation gives an easy interpretation of the space objects. However, most Earth-orbiting objects are too small or remote to be imaged by even the most advanced ground station resources.

A more implicit yet versatile method is a light curve inversion technique. The light curve is a time history of the photometric intensity of light reflected off an object, which is available even from higher orbits including geosynchronous orbits. The light curve inversion aims to estimate an object's shape, surface properties, or attitude based on its light curve. The initial work focused on celestial objects' characterization and successfully obtained a three-dimensional shape of asteroids [19; 20]. Recently, several studies have been carried out on characterizing artificial objects. Calef et al. [7] reconstructed the three-dimensional shape of an object based on its thermal emissions and light curve, assuming the known observer position and convexity of the object. Linares et al. [23] used the Unscented Kalman filter to determine the most probable shape out of predefined geometry models, based on the angles data and light curves. Linares and Crassidis [22] adopted the Bayesian inversion approach to recover the space object's shape and surface parameters. In the recent development of the deep learning technique, machine learning has also been adopted to the light curve to classify the object shape [18; 3]. Fan, Friedman, and Frueh [15; 14; 17] implemented the light curve inversion considering the observation noise and conditions for obtaining a sufficient amount of data for inversion.

Although much improvement has been made for the light curve inversion problem, it is still challenging to simultaneously estimate attitude, shape, and surface parameters. Even when concentrating on the shape inversion problem

alone, the problem is ill-posed, which often has multiple solutions and ambiguities. Therefore, this research adopts an image processing technique to avoid this difficulty. The key technique used in this research is the so-called compressed sensing.

Compressed sensing (CS) is a signal compression theory, which is capable of recovering a compressed signal with a very high compression ratio even if the compressed signal is inaccurate and incomplete [8; 9; 11]. A signal is compressed as a linear measurement by using a so-called sensing matrix. The original signal can be reconstructed almost exactly by solving a convex optimization problem. The number of measurements required by CS is far fewer than those required by the traditional Shannon/Nyquist sampling theorem [26] and hence CS has brought a paradigm shift in the signal processing field. There are several applications in aerospace engineering to enjoy this benefit. Aguilera et al. [1; 2] used CS to improve the performance of the synthetic aperture radar (SAR) tomography. Daponte et al. [10] used the CS framework to design radio frequency sensors to localize and track non-cooperative objects. Yokoya and Iwasaki [31] used the CS framework for object detection and classification in optical remote sensing images.

In the previous work by the authors [21], a similarity between the light curve measurement and compressed sensing has been investigated. Assuming that an object is stabilized in a known orbit, the object's light curve may be regarded as the object image compressed by atmospheric noise. The atmospheric noise in this model works as a sensing matrix in the CS framework. In the previous work, simultaneous observation of a known satellite is utilized to estimate the sensing matrix, and a resolved image of the observed object is successfully reconstructed.

This paper first re-examines the atmospheric noise model from a physical perspective and shows some limitations. Alternatively, the shadowing on the satellite is modeled as a sensing matrix, and compressed sensing is utilized to recover a net of the object. The net is a two-dimensional figure that can be folded into the original three-dimensional object, and it is adopted to accommodate the multiple viewing directions. This research shows the resolved image of the net can be successfully recovered from the object's light curve, assuming the sensing matrix is known.

The organization of this paper is as follows. First, theories of compressed sensing and its physical representation using a single-pixel camera are introduced. Second, the simulation scheme of a light curve is summarized. Third, the previous method using the atmospheric noise is summarized, and its physical validity is discussed. Finally, the alternative method considering shadowing is introduced. Two scenarios are tested according to the scheme of generating the sensing matrix.

2. COMPRESSED SENSING

2.1. Theory

In compressed sensing, a signal is sampled directly in a compressed form:

$$\mathbf{y} = \mathbf{\Phi x} \tag{1}$$

where $\mathbf{x} \in \mathbb{R}^N$ is a signal vector, $\mathbf{y} \in \mathbb{R}^M$ $(M \ll N)$ is a measurement vector, and $\mathbf{\Phi} \in \mathbb{R}^{M \times N}$ is a so-called sensing matrix. The sensing matrix compresses the signal by mapping a high-dimensional vector into a lower-dimensional vector. This leads to a much shorter sampling rate than that of the classical Shannon/Nyquist sampling theorem [26].

There a two keys to the success of compressed sensing. First, a signal $\mathbf{x}$ needs to be sparse in terms of a dictionary $\mathbf{\Psi}$ that captures the sparse structure of the signal:

$$\mathbf{x} = \mathbf{\Psi}\gamma + \mathbf{e} \tag{2}$$

where $\mathbf{\Psi} \in \mathbb{R}^{N \times L}$. The vector γ is a sparse vector and it satisfies $\|\gamma\|_0 \leq K$ with $K \ll N \leq L$. Note that $\|\cdot\|_0$ denotes the number of nonzero entries of a vector. The term $\mathbf{e}$ is the sparse representation error (SRE), which almost always exists for the practical signals of interest.

Another key element is a sensing matrix $\mathbf{\Psi}$. It is chosen so that the useful information in the signal $\mathbf{x}$ is preserved. For a stable reconstruction, an equivalent dictionary $\mathbf{\Phi\Psi}$ needs to satisfy a measure called Restricted Isometry Property (RIP) [12]. However, verifying whether a general matrix meets the RIP is an NP-hard problem [4]. Nevertheless, Baraniuk [5] showed that most random matrices satisfy the RIP. There are also some well-known and widely-used sensing matrices such as a Gaussian matrix, a Fourier transform matrix, and a Hadamard matrix.

Finally, the reconstruction method in compressed sensing is briefly summarized. Due to the fact that $M \ll N$, solving Equation 1 in terms of $\mathbf{x}$ is an ill-posed problem. However, if the signal $\mathbf{x}$ is sparse in terms of the dictionary $\mathbf{\Psi}$, and if the sensing matrix $\mathbf{\Phi\Psi}$ satisfies the RIP, then the signal $\mathbf{x}$ is guaranteed to be recovered from the measurement $\mathbf{y}$. This reconstruction is implemented by solving either of the following optimization problems:

$$\hat{\gamma} = \arg\min_{\gamma} \|\mathbf{y} - \mathbf{\Phi\Psi}\gamma\|_2 \quad \text{s.t. } \|\gamma\|_0 \leq K \tag{3}$$

$$\hat{\gamma} = \arg\min_{\gamma} \|\gamma\|_0 \quad \text{s.t. } \|\mathbf{y} - \mathbf{\Phi\Psi}\gamma\|_2 \leq \varepsilon \tag{4}$$

Equation 3 minimizes the SRE under the sparsity constraint, while Equation 4 minimizes the sparsity under the SRE constraint. The most well-known solver of these problems is the orthogonal matching pursuit (OMP) algorithm. In this research, the batch-OMP algorithm [28] is chosen because of its fast computation and well-known stability condition.

2.2. Single-Pixel Camera

One important CS application to understand the similarity with the light curve is a single-pixel camera [29]. In compressed sensing, a signal is linearly transformed by a sensing matrix. With a closer look at Equation 1, each entry of the measurement vector, y_i is computed as an inner product between a row of the sensing matrix, ϕ_i^T and the signal $\mathbf{x}$. Suppose the length of the signal $\mathbf{x}$ is n^2, the vectors ϕ_i^T and $\mathbf{x}$ can be reshaped into square matrices $\mathbf{\Phi}_i$ and $\mathbf{X}$ respectively. The entry $\mathbf{y}_i$ is a summation of the element-wise product between these two matrices:

$$\mathbf{y}_i = \phi_i^T \mathbf{x} = \sum \mathbf{\Phi}_i \odot \mathbf{X} \tag{5}$$

where $\odot$ denotes the element-wise product. Equation 5 suggests that the measurement vector $\mathbf{y}$ can be obtained by repeating the element-wise product m times. This idea is practiced in a single-pixel camera.

Figure 1 shows a schematic diagram of the single-pixel camera. In this camera, a scene is focused on a digital micromirror device (DMD) by a convex lens, and a photodiode collects the reflected light. The DMD array is a mirror grid consisting of millions of micromirrors, each of which reflects the light in two directions. Only the micromirrors that are oriented in one of the directions reflect the light toward the photodiode. One can see that the DMD works as a binary alternative of the sensing matrix, and it performs the measurement denoted by Equation 5. Therefore, the measurement is repeated m times with different mirror patterns in DMD to get a measurement vector $\mathbf{y}$, and the original scene is reconstructed by a CS solver. As a result, this camera is capable of imaging a scene with only a single photodiode.

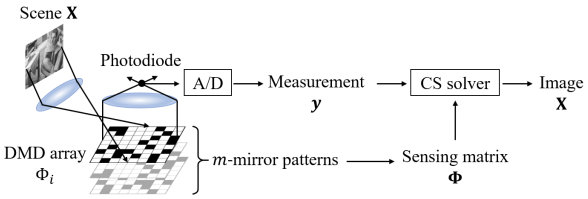

Figure 1: Single-pixel camera diagram

3. LIGHT CURVE SIMULATION

A light curve is a time series of the photometric intensity of an observed object [30]. It depends on the geometric shape, reflectance, and the relative position of the object to the Sun and the observer. In the light curve simulation, a space object is modeled as a polygon consisting of triangular meshes. First, the visibility of each mesh is determined by considering three possible cases where a mesh is invisible from the observer. Figure 2 shows a schematic of the three conditions. The first case is the mesh local horizon condition. The Sun and the observer must be above the local horizon of the mesh. The second case is the self-shadowing in which the light coming into a mesh is obstructed by another mesh. The third case is the observer-shadowing in which the light reflected off a mesh is obstructed by another mesh. These shadowing conditions are analyzed by a classical ray tracing algorithm [25].

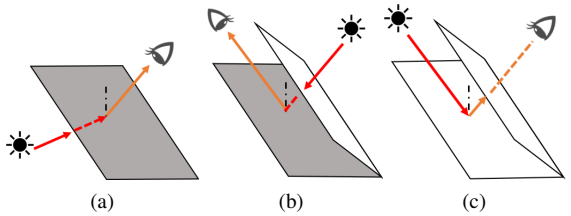

Figure 2: Three shadowing conditions checked in the light curve simulation. (a): mesh local horizon, (b): self-shadowing, (c): observer-shadowing

After screening out invisible meshes, the light intensity of each visible mesh is computed by the bi-directional reflectance distribution function (BRDF) model that consists of the Lambertian reflection term and the specular reflection term. The light intensity at time t_i is given by:

$$I_i = I_0 \sum_{j=1}^{n} \frac{\mu_{i,j} A_j}{\pi (r_{\text{topo},i})^2} (\hat{\mathbf{N}}_{i,j} \cdot \hat{\mathbf{S}}_i) \cdot \left\{ C_{d,j} (\hat{\mathbf{N}}_{i,j} \cdot \hat{\mathbf{V}}_i) + \frac{\pi \tau_{i,j} C_{s,j} (r_{\text{Sun}})^2}{(a_{\text{Sun},i})^2} \right\} \tag{6}$$

where the subscript i denotes the time index and j denotes the mesh index. The constant I_0 is the solar irradiance at 1 AU, n is the number of meshes, A is the mesh area, and r_{topo} is the distance between the object and observer. The coefficient μ denotes a mesh's visibility condition and is 1 only when the mesh is visible and otherwise 0. The vector $\hat{\mathbf{N}}$ is the mesh normal, $\hat{\mathbf{S}}$ is the object-to-the-Sun vector, and $\hat{\mathbf{V}}$ is the object-to-the-observer vector. These three vectors are normalized to unity. The parameter C_d is the diffuse reflection parameter, and C_s is the specular reflection parameter. The specular reflection is a mirror-like reflection that is concentrated in a particular direction. However, due to the finite size of the Sun, it allows half a degree difference between the incoming and the outgoing light. This condition is denoted by the coefficient τ as below:

$$\tau_{i,j} = \begin{cases} 1, \text{ if } \arccos \left\{ \frac{\hat{\mathbf{V}}_i + \hat{\mathbf{S}}_i}{|\hat{\mathbf{V}}_i + \hat{\mathbf{S}}_i|} \cdot \hat{\mathbf{N}}_{i,j} \right\} \leq 0.25^o \\ 0, \text{ o.w.} \end{cases} \tag{7}$$

In Equation 6, the finite extent of the Sun is computed by the solar radius r_{Sun} and the solar distance a_{Sun}.

By convention, the intensity is not directly used as a measure of the brightness. Alternatively, the brightness measured in a log scale is usually used. This is called a rela-

tive magnitude, and it is given by

$$\text{mag}(t_i) = \text{mag}_{\text{Sun}} - 2.5 \log_{10}\left(\frac{I_i}{I_0}\right) \quad (8)$$

where $\text{mag}_{\text{Sun}} = -26.74$, and I_0 is the solar intensity. Because of this definition, a brighter object has a smaller relative magnitude.

As an example, a light curve simulation has been implemented as follows. The ASTRA 1KR satellite is used as an object model with the reflection parameters, $C_d = 0.8$ and $C_s = 0.2$, assuming that the satellite is covered by aluminum. The satellite is propagated by SGP4 in a geosynchronous orbit based on the TLE data from the initial epoch, 0:00:00 AM on 1-April-2020 UTC for 1437 minutes. The observer is located in Berlin at 51.17^o N, 10.45^o E. Along with the light curve, the synthetic satellite images are also generated by orthogonal projection of the mesh brightness onto an image plane.

Figure 3 shows the simulated light curve and synthetic satellite images at five points of the light curve. It can be seen that the shadow cast on the satellite triggers a sudden change in the brightness.

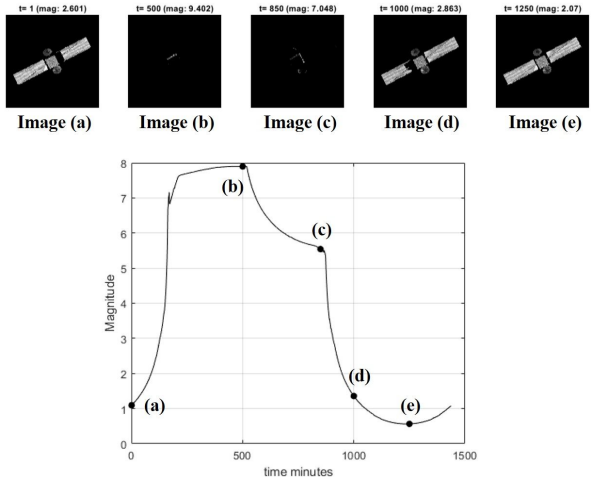

Figure 3: Simulated light curve and corresponding synthetic satellite images

4. ATMOSPHERE-BASED APPROACH

4.1. Atmospheric Noise as a Sensing Matrix

In the previous work by the authors [21], the light curve measurement is compared with a single-pixel camera. Figure 4 shows a comparison between these two measurements. In a single-pixel camera, the pixel values of the scene are projected onto the mirror pattern of the DMD, randomly weighted, and summed up by a photodiode. Similarly, in a light curve measurement, the light rays from each part of the satellite pass through the atmosphere and hence attenuated randomly before reaching the ground station. This random attenuation due to the atmosphere is similar to the projection onto the DMD. Subsequently, the attenuated light rays are collected by telescope, which is similar to the measurement by a photodiode. Assuming that the satellite is observed in a short time such that it is regarded as a still image, m measurements of the satellite with m different atmospheric noise are analogous to the m measurements with m different mirror patterns on DMD. Therefore, the light curve measurement can also be modeled by Equation 1.

Based on this similarity, the previous work has introduced an adapted light curve model. In this model, the atmospheric attenuation is considered a sensing matrix, and the light curve is considered an image compressed by an unknown sensing matrix. Since the atmospheric attenuation is usually unknown, it has been estimated by implementing the simultaneous observations of a known satellite. As a result, a resolved satellite image has been successfully reconstructed.

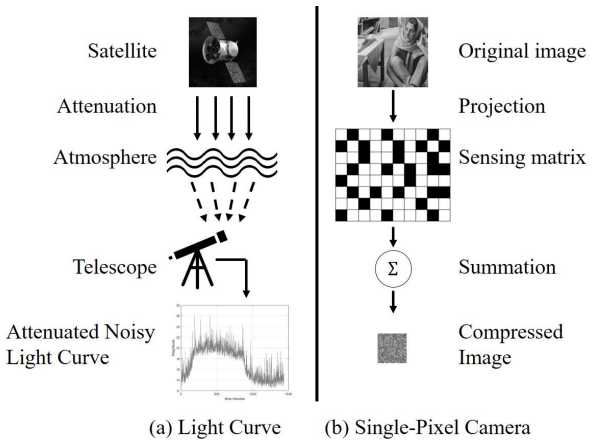

Figure 4: Comparison between a light curve and a single pixel camera: (a) observation of a light curve attenuated by atmosphere, (b) observation by a single-pixel camera

4.2. Validity of the Atmosphere-based Approach

The previous method is based on the assumption that the light rays from each part of the satellite pass through the different parts of the atmosphere, and they are attenuated by different factors. This helps the sensing matrix distinguish one part of the satellite from another part in the reconstruction process. In this research, this assumption is tested based on atmospheric disturbance theory.

First, the required separation of the light rays is computed in terms of the isoplanatic angle. The isoplanatic angle is the maximum angular separation between objects such that the turbulence-induced wavefront deformations for these objects are reasonably similar [27]. The previous

method requires that the light rays pass through atmospheric patches separated apart by this isoplanatic angle. This angle is defined by Fried [16] as:

$$\theta_0 = 58.1 \times 10^{-3} \lambda^{6/5} \left[\int_0^L C_n^2(z) z^{5/3} dz \right]^{-3/5} \quad (9)$$

where λ is the optical wavelength, L is the path length through turbulence, and $C_n^2(z)$ is the structure constant of the turbulence that characterizes the strength of the index of refraction fluctuations. At visible wavelengths, typical values of θ_0 are 5-10 μrad. Suppose the altitude of the top atmospheric layer is around $L = 50$km, then the isoplanatic patch size is

$$\Delta x_0 \approx L\theta_0 \approx 0.5m \quad (10)$$

Second, the resolution of the light rays is considered. The Rayleigh criterion [6] states the smallest angular separation of two objects that can be resolved in a circular aperture is given by

$$\Delta\theta \approx 1.22 \frac{\lambda}{a} \quad (11)$$

where a is the aperture diameter in meters. Using this criterion, the minimum spatial separation of an observed object is computed by

$$\Delta x \approx R\Delta\theta \approx 1.22 \frac{\lambda R}{a} \quad (12)$$

where R is the distance between the object and the aperture. Based on this criterion, the minimum spatial separation of an object in geosynchronous orbit is computed. Suppose the telescope is outside of the atmosphere at an altitude of 1000 km, then the distance is around $R \approx 35{,}000$ km. Recall that the isoplanatic patch size is 0.5 m as shown in Equation 10, it is assumed that the telescope has an aperture of the same size: $a = 0.5$m. Suppose the optical wavelength is $\lambda = 500$ nm, the minimum spatial separation is computed as 42.7 m. Given that most geosynchronous satellites are around 10 m, the light rays from the satellites are not resolved even by the telescope. This result suggests that all the light rays would go through the same isoplanatic patch, and they would be attenuated homogeneously.

The discussions above suggest that the light rays from each part of the satellite are attenuated by the same factor. This corresponds to a single-pixel camera where all the micromirrors are oriented in one particular direction, and hence it is impossible to distinguish each light ray. Therefore, the reconstruction of a resolved image based on a light curve does not work for geosynchronous satellites.

On the other hand, if a target satellite is in a lower orbit such that the light rays do not converge before the atmosphere, this method would work. However, a resolved or semi-resolved image of a satellite is already available for objects in this region, so it is not advantageous to apply our method. Nevertheless, compressed sensing could be beneficial to remove atmospheric distortions of such images.

5. SHADOWING-BASED APPROACH

5.1. Shadowing as a Sensing Matrix

This research proposes an alternative method to obtain a resolved image of satellites in a high orbit. In this method, a shadow cast on the satellite is compared with the sensing matrix. Figure 5 shows a comparison between this model and a single-pixel camera. Without considering the visibility conditions, light rays from all the meshes are observed by a telescope. However, as mentioned earlier in Section 3, some meshes are not observed due to the mesh local horizon, observer-shadowing, and self-shadowing. One can see that these shadowing conditions attenuate the light intensity that is supposed to be observed. Since this attenuation changes with time and variant over the meshes, it is somewhat similar to the compression by sensing matrix. This new approach using shadowing as a sensing matrix is referred to as a shadowing-based approach in this paper.

The shadowing-based approach needs an adapted image model to accommodate the new sensing matrix. A typical method to render an image in computer graphics is an orthogonal projection of a 3D model onto a 2D observer plane. This rendering technique has been used in the previous method assuming a constant satellite attitude and shadowing conditions during the observation. However, this rendering method is not suitable in the shadowing-based approach because various shadowing conditions change the image over time, which is not suitable for compressed sensing. Therefore, this research proposes an adapted image called net image to accommodate the various shadowing conditions.

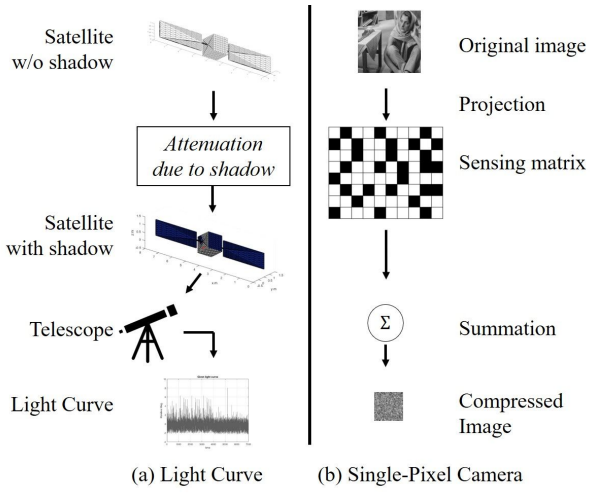

Figure 5: Comparison between a light curve and a single pixel camera: (a) observation of a light curve attenuated by shadow, (b) observation by a single-pixel camera

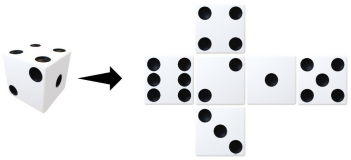

Figure 6: Die and its net

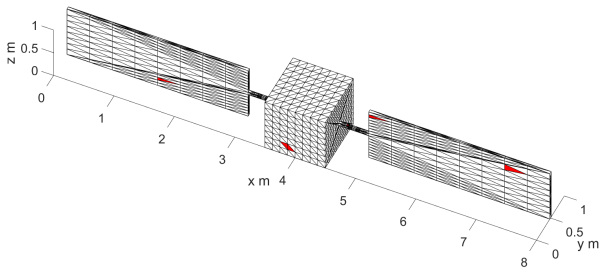

(a) Generic satellite model

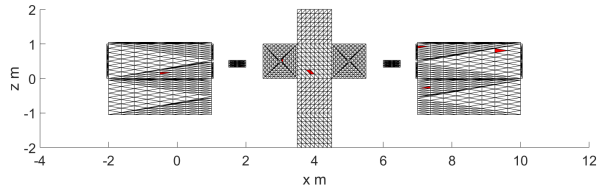

(b) Net of the satellite model

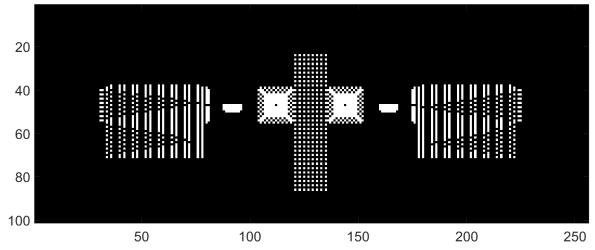

(c) Net image of the satellite model

Figure 7: Generic satellite model and corresponding net and net image

A net is a 2D figure that can be folded into its original 3D figure. Figure 6 shows one example of the net. Its biggest advantage is that all meshes are visible regardless of the satellite attitude and shadowing conditions. In this research, a generic box-wing satellite model as shown in Figure 7a is considered. This satellite model consists of a bus, two solar panels, and two supporting rods connecting the panels and the bus. All these components are simplified as cuboids made up of nil thickness rectangular facets. In each component, the facets are unfolded along the crease so that all the facets are on the zx-plane. The resultant nets of the components are then located so that they have no overlaps. Figure 7b shows the generated net of the satellite. Several meshes of the net marked in red correspond to the red meshes in the satellite model. Finally, the net is converted to an image by sampling each mesh center by image grid. The coordinates of the net are stretched to fit into the image of size 100×256, and then mesh center positions are rounded and assigned to pixels. The pixel value is 1 if a mesh is assigned but otherwise 0. This binary image is referred to as a net image in this paper. Figure 7c shows the net image of the satellite obtained from Figure 7b.

In the conversion from the net to the net image, the mapping between the meshes and pixels needs to be recorded carefully. Some meshes on the net are very close to each other, and hence they are mapped to the same pixel on the net image. This correspondence relationship will be used in the computation of the sensing matrix in a later section.

5.2. Assumptions in Shadowing-Based Approach

In this research, the net image of the satellite is estimated by a compressed sensing scheme. Let $\mathbf{X}$ denote the net image, and then it is reshaped into a vector $\mathbf{x}$. The light curve measurement at m time steps is given by

$$\mathbf{y} = \mathbf{\Phi x} \tag{13}$$

where the (i, j)-th entry of the sensing matrix $\mathbf{\Phi}$ is

$$\mathbf{\Phi}_{i,j} = \begin{cases} 0 & \text{if } j\text{-th mesh is invisible at time } t_i \\ \phi_{i,j} & \text{if } j\text{-th mesh is visible at time } t_i \end{cases} \tag{14}$$

where $\phi_{i,j}$ corresponds to the brightness of the j-th mesh at time t_i:

$$\begin{aligned} \phi_{i,j} = & \frac{A_j}{\pi (r_{\text{topo},i})^2} (\hat{\mathbf{N}}_{i,j} \cdot \hat{\mathbf{S}}_i) \\ & \cdot \left\{ C_{d,j} (\hat{\mathbf{N}}_{i,j} \cdot \hat{\mathbf{V}}_i) + \frac{\pi \tau_{i,j} C_{s,j} (r_{\text{Sun}})^2}{(a_{\text{Sun},i})^2} \right\} \end{aligned} \tag{15}$$

Note that the expressions above are directly obtained from Equation 6.

The sensing matrix in this model characterizes the shadowing condition on the meshes at each time step. In this study, two assumptions are made about the sensing matrix. First, the positions of the Sun, observer, and the satellite are assumed to be known. Since most characterization methods start from tracking the object, this would be a fair assumption. Therefore, in Equation 15, the variables $r_{\text{topo},i}$, $\hat{\mathbf{S}}_i$, $\hat{\mathbf{V}}_i$, and $a_{\text{Sun},i}$ are known.

Second, the shape-dependent parameters: A_j, $\hat{\mathbf{N}}_{i,j}$, $C_{d,j}$, $C_{s,j}$ are also assumed. In reality, they are not available because it is the information of interest. Thus, there seems to be no straightforward way to know the sensing matrix beforehand, even though compressed sensing necessitates it. However, the focus of this research is placed on validating this shadowing-based approach. In the first place, it is not yet validated whether the shadowing works

as a sensing matrix. Therefore, this research investigates the feasibility of this model given a sensing matrix. The unavailability of the sensing matrix will be handled in future work by a simultaneous estimation of the sensing matrix and the net image.

6. SIMULATION

In the following, the reconstruction of a net image of a satellite by compressed sensing is simulated under two scenarios. The first scenario is an idealized simulation where the sensing matrix is designed to follow the RIP condition strictly. The second scenario tests a more realistic case where the sensing matrix is computed based on the light curve simulation. Figure 8 shows the procedure for the simulations.

In both cases, given the light curve and sensing matrix, the following compressed sensing problem is solved by batch-OMP algorithm:

$$\hat{\mathbf{x}} = \arg\min_{\mathbf{x}} \|\mathbf{x}\|_0 \quad \text{s.t. } \|\mathbf{y} - \mathbf{\Phi}\mathbf{x}\|_2 \leq \varepsilon \tag{16}$$

Note that a dictionary is not used because the image signal itself is sparse. The error bound ε is set to be 0.1 based on several experiments. The solution of Equation 16 is then binarized to get a net image. The threshold is determined by an iterative way such that the number of pixels above the threshold does not exceed $3{,}000$.

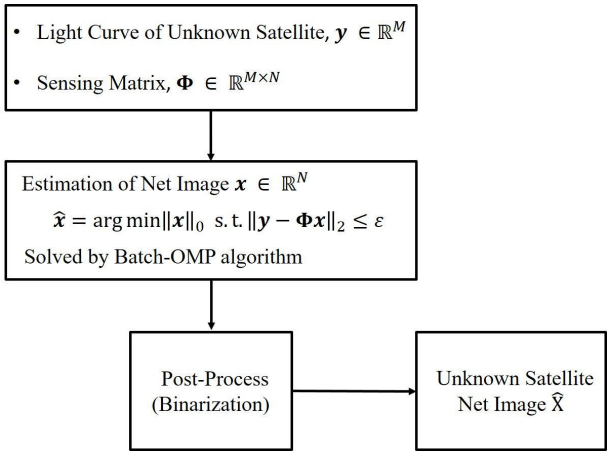

Figure 8: Flowchart of the simulations

6.1. Sensing Matrix with Random Binary Entries

In this simulation, the idea of the shadowing-based approach is tested under idealized conditions. The sensing matrix is generated by choosing either 0 or 1 randomly. In each row, the number of zeros is restricted so that the sensing matrix does not hide more than 80% of the non-zeros of the original net image. Note that the size of the original net image is 100×256, and it has $K(= 1{,}684)$ non-zero entries. The number of rows of the sensing matrix is $M(= 1{,}800)$.

This simulation does not consider any physical restrictions on the shadow due to the 3D structure of the satellite. In other words, $\phi_{i,j}$ is restricted to 1 in Equation 14, and the visibility condition is not also considered. Each measurement corresponds to the random pixel hiding of the original net image. The pixel summation of the corrupted net image is computed as the intensity of the light curve.

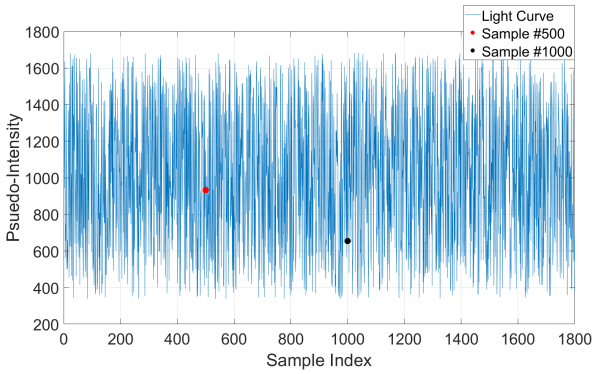

(a) Simulated light curve

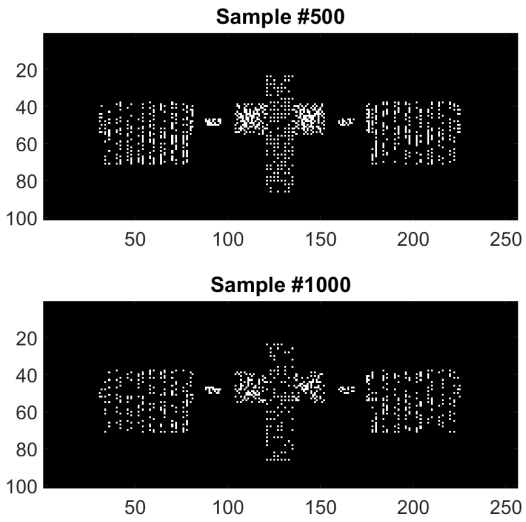

(b) Examples of corrupted net image

Figure 9: Simulated light curve and two sample net images in the first simulation

Figure 9a shows the light curve obtained in this simulation. The horizontal axis shows the indices of the samples, and the vertical axis shows the pseudo-intensity, which is equal to the pixel sum of the corrupted net image in each measurement. Figure 9b shows the corrupted net images of the 500th and 1000th sample. As can be seen, the pixel values are randomly hidden by the sensing matrix. The hidden pixels are located uniformly throughout the images, and they do not reflect the actual shadow

pattern.

Figure 10 shows the result of this simulation. The reconstructed net image has all the non-zero entries of the original net image, although it has one redundant non-zero element. The result is almost perfect because the sensing matrix follows the RIP condition strictly because of its randomness.

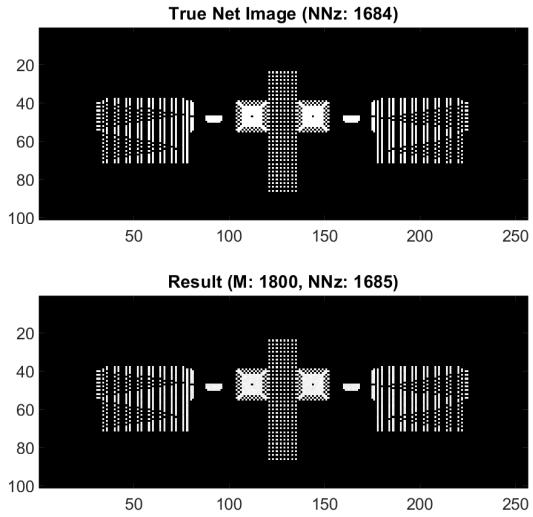

Figure 10: Comparison of true net image and result of the first simulation with sensing matrix with random binary entries

6.2. Sensing Matrix by Ray Tracing

In this simulation, the shadowing-based approach is tested by actual shadowing conditions. The entries of the sensing matrix are determined so that it follows Equation 14 and 15. In the following, the procedures for computing the sensing matrix are explained.

First, the light intensity of all the meshes of the 3D satellite model is computed. The satellite model in Figure 7a is observed from a random direction with a random sunlight direction while the range is fixed to 100 km. Note that the intensity of the meshes invisible due to mesh local horizon, observer-shadowing, and self-shadowing is computed as 0. This computation gives an intensity vector of length n that stores the intensity of all the n facets of the satellite at time t_i. The summation of the entries, y_i is the light intensity at this time step.

Second, the i-th row of a sensing matrix, $\phi_i^T \in \mathbb{R}^N$ is computed based on the intensity vector where N is the total number of pixels of the net image. First, the vector ϕ_i^T is initialized by zeros. As mentioned in the analogy with a single-pixel camera, each entry of ϕ_i^T attenuates the net image in a pixel-wise way. Suppose the net image has non-zero entries in the pixels indexed by $\mathcal{I}$, then the entries of the intensity vector are assigned to the indices $\mathcal{I}$ of ϕ_i^T. It is important to note that some intensity values are mapped to the same entry of ϕ_i^T. In this case, the sum of all the intensity values corresponding to that pixel is assigned to the entry of ϕ_i^T.

Subsequently, the entries of the vector ϕ_i^T outside of the indices $\mathcal{I}$ are considered. Let ϕ_{bg} denote the corresponding entries. In the measurement $\mathbf{y} = \mathbf{\Phi x}$, these entries are multiplied by the background entries of the net image $\mathbf{x}$, which are zero. Thus, the entries of the vector ϕ_{bg} are canceled by multiplication and they do not affect the light curve intensity $\mathbf{y}$. However, to avoid the all-zeros column in the sensing matrix, arbitrary non-zero values need to be assigned to those entries. In this research, the Gaussian entries of mean 0 and standard deviation 1×10^{-10} are generated and assigned to ϕ_{bg}.

These procedures are repeated for $M(= 7{,}000)$ times to obtain the light curve $\mathbf{y} \in \mathbb{R}^M$ and sensing matrix $\mathbf{\Phi} \in \mathbb{R}^{M \times N}$.

This simulation considers the shadow in a physically more accurate way than the first simulation. However, this leads to the less random entries of the sensing matrix. Since randomness is one requirement to satisfy the RIP condition, it may result in the worse performance of compressed sensing.

Figure 11a shows the light curve obtained in this simulation. The horizontal axis shows the indices of the samples, and the vertical axis shows the magnitude of the light curve computed by Equation 8. Figure 11b shows the satellite model corresponding to the 2001st and 5213th sample, respectively. In both cases, the red arrow shows the direction of the light, and four different colors display the visibility of each facet. The direction of the observer is oriented out of the paper. Figure 11c shows the corresponding nets of these two samples. Similarly, the visibility of each facet is displayed by four different colors. Clearly, the shadow patterns are totally different from that of Figure 9b. The shadow tends to be less variant and less random because of the more realistic setup, especially on the solar panels. However, the shadow on the side panels of the bus component tends to be variant because of the self-shadowing and observer-shadowing cast by the supporting rods.

Figure 12 shows the result of this simulation. The number of non-zero pixels of the result is only 322, about 19% of the correct net image's total non-zero entries. However, even this incomplete result gives enough implication for characterizing the shape of an unknown satellite. With a closer look, the side panels of the bus part are reconstructed better than the other parts. On the other hand, the solar panels are reconstructed less accurately. These results imply that the randomness of the shadowing improves the performance of the sensing matrix. This result is reasonable because the randomness gives the better RIP condition. Therefore, surprisingly, the shadowing-based approach would give a better reconstruction result for a more complex satellite model due to the increased

randomness in the shadow. This characteristic of the shadowing-based approach is counter-intuitive and different from the most previous light curve inversion schemes.

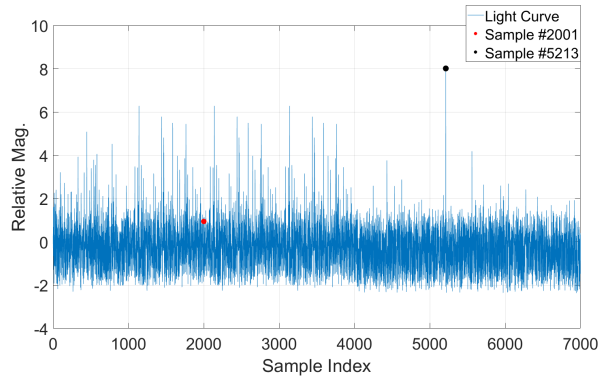

(a) Simulated light curve

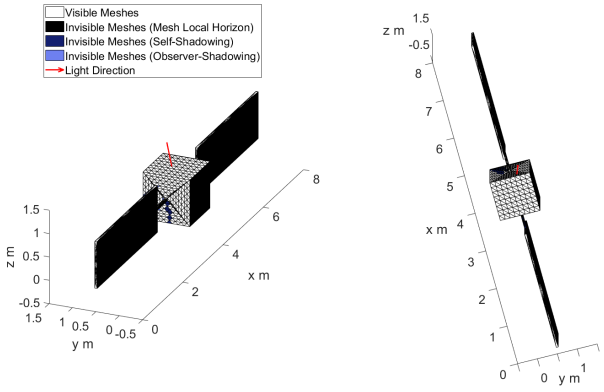

(b) Appearance of satellite models in the 2001st and 5213th samples

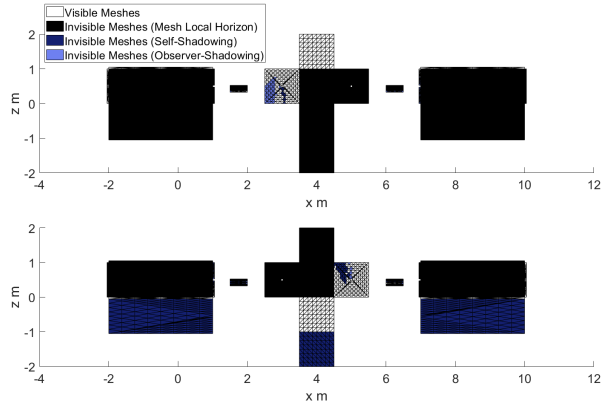

(c) Satellite nets of the 2001st and 5213th samples

Figure 11: Simulated light curve and two samples in the second simulation. (a): simulated light curve, (b): light directions and attitudes of satellite models corresponding to two samples, where the observer's direction is oriented out of the paper, (c) satellite nets of the two samples

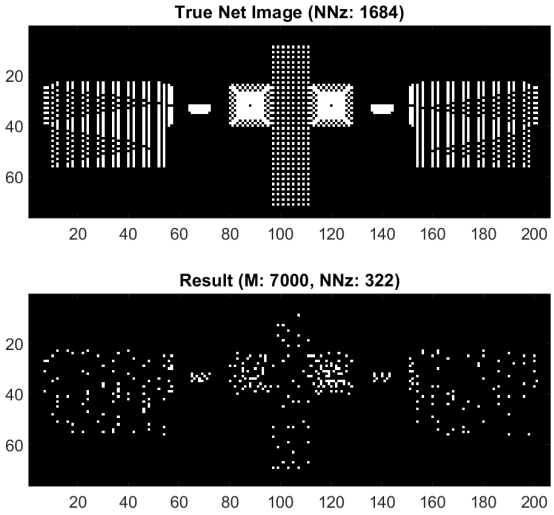

Figure 12: Comparison of true net image and result obtained with sensing matrix by Ray Tracing

7. CONCLUSIONS AND FUTURE WORK

This research has discussed a potential application of compressed sensing to characterize an unknown stabilized satellite in a known orbit from its non-resolved light curve. Compressed sensing is a mathematical theory for efficient signal compression and reconstruction. The signal is compressed by a linear transformation by a random matrix, which is referred to as a sensing matrix. In this research, it has been compared with light curve measurements from two perspectives.

The first model considers the atmospheric turbulence as a pseudo-sensing matrix, and the light curve is considered an image compressed by the unknown sensing matrix. This approach gives a resolved image of an unknown satellite, which is detailed in the authors' previous work. This research has discussed the validity of this model in terms of the isoplanatic patch size and the Rayleigh criterion. It has been found that the light rays from geosynchronous satellites converge to one light ray before reaching the atmosphere, and they are not distinguishable in the reconstruction process. Therefore, this atmosphere-based approach works only for satellites in low Earth orbits where a resolved or semi-resolved image is already available by telescope observation.

This research has proposed an alternative method to reconstruct a net of a target satellite. This model considers a shadow on a satellite as a sensing matrix because each facet's light intensity is attenuated by the shadow somewhat randomly. This model is tested in two scenarios assuming that the sensing matrix is known. In the first case, the sensing matrix has random binary entries that hide random parts of the satellite net. In this case, the

satellite net has been reconstructed almost perfectly because the sensing matrix has perfectly random entries. In the second case, the sensing matrix has been generated based on a light-curve simulation. The light curve is simulated by observing a 3D satellite model with 7,000 random sets of viewing direction and light direction. This brings some randomness in the sensing matrix, but the shadow pattern is less varied than in the first case. Therefore, the result gets worse than that of the first simulation, and only 19% of the non-zero entries are recovered. However, the result gives enough insight into the original satellite shape. Moreover, the poor performance of the reconstruction is due to a simple structure of the generic satellite model used in the simulation, which does not cast a variety of shadow patterns. This suggests a surprising and counter-intuitive implication that the proposed method would work better for a satellite with a complex structure that causes more random shadow patterns.

Future work will focus on relaxing the assumptions in the shadowing-based approach. The light curve will be simulated under more realistic conditions by assuming a specific orbit of the satellite. Furthermore, a co-estimation method of the sensing matrix and the satellite net will be investigated to eliminate the need for prior knowledge of the sensing matrix. Moreover, reconstruction of an image or a more user-friendly alternative to the net image will also be considered.

REFERENCES

1. AGUILERA, E., NANNINI, M., AND REIGBER, A. Multisignal compressed sensing for polarimetric sar tomography. *IEEE Geoscience and Remote Sensing Letters 9*, 5 (2012), 871–875.
2. AGUILERA, E., NANNINI, M., AND REIGBER, A. Wavelet-based compressed sensing for sar tomography of forested areas. *IEEE transactions on geoscience and remote sensing 51*, 12 (2013), 5283–5295.
3. ALLWORTH, J., WINDRIM, L., BENNETT, J., AND BRYSON, M. A transfer learning approach to space debris classification using observational light curve data. *Acta Astronautica 181* (2021), 301–315.
4. BANDEIRA, A. S., DOBRIBAN, E., MIXON, D. G., AND SAWIN, W. F. Certifying the restricted isometry property is hard. *IEEE transactions on information theory 59*, 6 (2013), 3448–3450.
5. BARANIUK, R., DAVENPORT, M., DEVORE, R., AND WAKIN, M. A simple proof of the restricted isometry property for random matrices. *Constructive Approximation 28*, 3 (2008), 253–263.
6. BORN, M., AND WOLF, E. *Principles of optics: electromagnetic theory of propagation, interference and diffraction of light*. Elsevier, 2013.
7. CALEF, B., AFRICANO, J., BIRGE, B., HALL, D., AND KERVIN, P. Photometric signature inversion. In *Unconventional Imaging II* (2006), vol. 6307, International Society for Optics and Photonics, p. 63070E.
8. CANDÈS, E. J., ET AL. Compressive sampling. In *Proceedings of the international congress of mathematicians* (2006), vol. 3, Madrid, Spain, pp. 1433–1452.
9. CANDES, E. J., ROMBERG, J. K., AND TAO, T. Stable signal recovery from incomplete and inaccurate measurements. *Communications on Pure and Applied Mathematics: A Journal Issued by the Courant Institute of Mathematical Sciences 59*, 8 (2006), 1207–1223.
10. DAPONTE, P., DE VITO, L., PICARIELLO, F., RAPUANO, S., AND TUDOSA, I. Compressed sensing technologies and challenges for aerospace and defense rf source localization. In *2018 5th IEEE International Workshop on Metrology for AeroSpace (MetroAeroSpace)* (2018), IEEE, pp. 634–639.
11. DONOHO, D. L. Compressed sensing. *IEEE Transactions on information theory 52*, 4 (2006), 1289–1306.
12. ELAD, M. *Sparse and redundant representations: from theory to applications in signal and image processing*. Springer Science & Business Media, 2010.
13. ESA'S SPACE DEBRIS OFFICE. Space debris by the numbers. https://www.esa.int/Safety_Security/Space_Debris/Space_debris_by_the_numbers, 2021. Online; accessed 2 April 2021.
14. FAN, S., FRIEDMAN, A., AND FRUEH, C. Satellite shape recovery from light curves with noise. *amos* (2019), 23.
15. FAN, S., AND FRUEH, C. A direct light curve inversion scheme in the presence of measurement noise. *The Journal of the Astronautical Sciences* (2019), 1–22.
16. FRIED, D. L. Anisoplanatism in adaptive optics. *JOSA 72*, 1 (1982), 52–61.
17. FRIEDMAN, A., FAN, S., FRUEH, C., AND SCHILDKNECHT, T. Observability of light curve shape inversion based on optical data. In *First International Orbital Debris Conference* (2019).
18. FURFARO, R., LINARES, R., AND REDDY, V. Shape identification of space objects via light curve inversion using deep learning models. In *AMOS Technologies Conference, Maui Economic Development Board, Kihei, Maui, HI* (2019).
19. KAASALAINEN, M., AND TORPPA, J. Optimization methods for asteroid lightcurve inversion: I. shape determination. *Icarus 153*, 1 (2001), 24–36.
20. KAASALAINEN, M., TORPPA, J., AND MUINONEN, K. Optimization methods for asteroid lightcurve inversion: Ii. the complete inverse problem. *Icarus 153*, 1 (2001), 37–51.
21. KOBAYASHI, D., AND FRUEH, C. Compressed sensing for satellite characterization. AIAA/AAS Astrodynamics Specialist Conference.

22. LINARES, R., AND CRASSIDIS, J. L. Resident space object shape inversion via adaptive hamiltonian markov chain monte carlo. In *AAS/AIAA Space Flight Mechanics Meeting* (2016), pp. 2016–514.

23. LINARES, R., JAH, M. K., CRASSIDIS, J. L., AND NEBELECKY, C. K. Space object shape characterization and tracking using light curve and angles data. *Journal of Guidance, Control, and Dynamics 37*, 1 (2014), 13–25.

24. MEHRHOLZ, D., LEUSHACKE, L., FLURY, W., JEHN, R., KLINKRAD, H., AND LANDGRAF, M. Detecting, tracking and imaging space debris. *ESA Bulletin(0376-4265)*, 109 (2002), 128–134.

25. MÖLLER, T., AND TRUMBORE, B. Fast, minimum storage ray-triangle intersection. *Journal of graphics tools 2*, 1 (1997), 21–28.

26. NYQUIST, H. Certain topics in telegraph transmission theory. *Transactions of the American Institute of Electrical Engineers 47*, 2 (1928), 617–644.

27. ROGGEMANN, M. C., AND WELSH, B. M. *Imaging through turbulence*. CRC press, 1996.

28. RUBINSTEIN, R., ZIBULEVSKY, M., AND ELAD, M. Efficient implementation of the k-svd algorithm using batch orthogonal matching pursuit. Tech. rep., Computer Science Department, Technion, 2008.

29. TAKHAR, D., LASKA, J. N., WAKIN, M. B., DUARTE, M. F., BARON, D., SARVOTHAM, S., KELLY, K. F., AND BARANIUK, R. G. A new compressive imaging camera architecture using optical-domain compression. In *Computational Imaging IV* (2006), vol. 6065, International Society for Optics and Photonics, p. 606509.

30. WARNER, B. D., ET AL. *A practical guide to lightcurve photometry and analysis*, vol. 300. Springer, 2006.

31. YOKOYA, N., AND IWASAKI, A. Object detection based on sparse representation and hough voting for optical remote sensing imagery. *IEEE Journal of Selected Topics in Applied Earth Observations and Remote Sensing 8*, 5 (2015), 2053–2062.